

## AN INCOMPRESSIBLE NAVIER–STOKES MODEL IMPLEMENTED ON NONSTAGGERED GRIDS

*Tony W. H. Sheu and R. K. Lin*

*Department of Engineering Science and Ocean Engineering,  
National Taiwan University, Taipei,  
Taiwan, Republic of China*

*The present study aims to develop an effective finite-difference model for solving incompressible Navier–Stokes equations. For the sake of programming simplicity, discretization of equations is made on nonstaggered grids without oscillatory solutions arising from the decoupling of the velocity and pressure fields. For the sake of computational efficiency, both segregated and alternating direction implicit (ADI) solution algorithms are employed to reduce the matrix size and, in turn, the CPU time. For the sake of numerical accuracy, a convection-diffusion-reaction finite-difference scheme is employed to provide nodally exact solutions in each ADI solution step. The convective instability problem is thus eliminated, since each convective term is modeled analytically even in multidimensional cases. The validity of the proposed numerical model is rigorously justified by solving one- and two-dimensional problems, which are amenable to analytical solutions. The simulated solutions for the scalar prototype equation agree well with the exact solutions and provide a very high spatial rate of convergence. The same is true for the simulated results of the Navier–Stokes equations.*

### 1. INTRODUCTION

The numerical simulation of incompressible viscous flows remains an area of continuous importance owing to its wide range of industrial applications. A direct use of centered differences to discretize the advective terms in the flow equation is known to yield oscillations primarily in the velocity field. To eliminate this problem, one can use advective discretization schemes which possess the upwinding characteristics [1]. As the spatial dimension exceeds one, numerical approximation of these advective terms can, however, give rise to problems with false diffusion error [2]. Therefore, it is essential that the flux discretization scheme employed in this article dispense with this type of error without sacrificing scheme stability. To achieve this goal, splitting of equations is done so that solutions can be more

Received 16 September 2002; accepted 8 March 2003.

This work was supported by the National Science Council of the Republic of China under Grant NSC 88-2611-E-002-025.

Address correspondence to Tony W. H. Sheu, National Taiwan University, Department of Engineering Science and Ocean Engineering, 73 Chow-Shan Road, Taipei, Taiwan, Republic of China. E-mail: twhsheu@ntu.edu.tw

### NOMENCLATURE

$\text{erf}(m)$	error function	Re	Reynolds number ( $\equiv \rho u_\infty L/\mu$ )
$f$	boundary force per unit volume	$u_{\text{id}}$	characteristic velocity
$k$	diffusion coefficient defined in Eq. (7)	$u_\infty$	reference velocity
$k_m$	wave-number defined in Eq. (19)	$\alpha$	modified wave-number defined in Eq. (28)
$L$	characteristic length	$\nu$	Courant number defined in Eq. (24)
$n$	unit outward normal vector	$\rho$	fluid density
$Pe$	Peclet number defined in Eqs. (26–28)		

efficiently and accurately obtained using the analytical one-dimensional scheme described in Section 4.1. Another concurrent benefit is the saving of disk storage and computing time.

When simulating incompressible Navier–Stokes equations in primitive variables, checkerboard oscillations occur on a nonstaggered (collocated) grid if central difference is used to approximate the pressure gradient term in the momentum equation and the cell-face velocity in the continuity equation [3]. The oscillatory solution is a manifesting of two separate pressure solutions at alternating nodes. Such a node-to-node oscillatory solution pattern arises from decoupling of the velocity and pressure fields. This provided motivation for discretizing equations on a staggered grid. With the staggered mesh, it permits coupling of the  $u$ ,  $v$ , and  $p$  solutions at adjacent grid points and, in turn, prevents the appearance of oscillatory pressure solutions [4].

In the literature, there exist several approaches which can be used to resolve the checkerboarding problem without resorting to staggered grids. A representative example was given by Rhie and Chow [5], who interpolated the cell-face velocities by virtue of the momentum interpolation and approximated pressure gradient terms using the central differencing scheme. The enhanced discrete stability is attributed to the fourth-order dissipation added into the pressure field [6]. Because of its wider applicability, there are some variants of this original momentum interpolation method (MIM) (see, for example, [7–14]). The second class of nonstaggered approaches introduces the weighted upwinding interpolation to approximate the pressure gradient term. This idea was applied with success to a variety of flow problems [15, 16]. The consistent physical interpolation is the third class of methods developed to circumvent checkerboard oscillations in the pressure field. A significant contribution in this analysis is due to Schneider and Raw [17]. With some modifications, this method has been extended by Deng et al. [18, 19]. In the literature, there are several assessment studies of the collocated and staggered-grid approaches. Among these studies are the works of Peric et al. [20] and Melaen [21].

The need to suppress oscillations of different origins (velocity and pressure) without deteriorating prediction accuracy motivated the present study. In Section 2, the working equations in primitive variables are described along with implementation of boundary conditions for the pressure Poisson equation. This is followed by the presentation of the rationale for advocating the segregated solution algorithm on nonstaggered grids. In Section 4, the underlying convection-diffusion-reaction (CDR) alternating direction implicit (ADI) model is presented to solve the solution

of the transient momentum equations. In Section 5, validation of the model is accomplished by solving three problems, which are all amenable to analytical solutions. Finally, some conclusions are drawn in Section 6.

## 2. WORKING EQUATIONS

In this study we will restrict our attention to viscous incompressible flows, which are governed by the following continuity equation and the Navier–Stokes equations:

$$\nabla \cdot \mathbf{u} = 0 \quad (1)$$

$$\frac{\partial \mathbf{u}}{\partial t} + \mathbf{u} \cdot \nabla \mathbf{u} = -\nabla p + \frac{1}{\text{Re}} \nabla^2 \mathbf{u} + \mathbf{f} \quad (2)$$

The primitive variables are sought subject to the initially divergence-free velocity field and the boundary velocity. All lengths are scaled by  $L$ , the velocity components by  $u_\infty$ , the time by  $L/u_\infty$ , and the pressure by  $\rho u_\infty^2$ , where  $\rho$  denotes the fluid density. The Reynolds number  $\text{Re}(\equiv \rho u_\infty L/\mu)$  appears as a result of the above normalization.

Momentum conservation equations can be solved along with the divergence-free constraint equation (continuity equation), thereby unconditionally ensuring fluid incompressibility. Despite the widespread use of the coupled solution algorithm to solve the incompressible flow equations, the eigenvalues of the resulting matrix equation may be poorly distributed. The solutions are thus very difficult to obtain using a computationally less expensive iterative solver [22]. Besides this disadvantage, the amount of peripheral storage required for the global system of matrix equations can be excessive, typically exceeding the available computer power and disk space. This drawback may discourage use of the coupled formulation in favor of other, computationally less demanding methods. The well-known pressure Poisson equation (PPE) approach [23] was developed to eliminate pressure from the momentum equations by applying a curl operator. In this manner, the following Poisson equation for the pressure is derived in lieu of the divergence-free continuity equation (1):

$$\nabla^2 p = \nabla \cdot \left( -\frac{\partial \mathbf{u}}{\partial t} + \frac{1}{\text{Re}} \nabla^2 \mathbf{u} - \mathbf{u} \cdot \nabla \mathbf{u} + \mathbf{f} \right) \quad (3)$$

The above approach is not without complication, since a theoretically rigorous integral boundary condition for  $p$  must be used [24]. This is a trade-off between the benefit of gaining computational efficiency and the drawback of having to solve for the pressure using Eq. (3), subject to a computationally more challenging integral pressure boundary condition. For this reason, we adopt in this study the following Neumann-type pressure boundary condition [25]:

$$\frac{\partial p}{\partial \mathbf{n}} = \left( -\frac{\partial \mathbf{u}}{\partial t} + \frac{1}{\text{Re}} \nabla^2 \mathbf{u} - \mathbf{u} \cdot \nabla \mathbf{u} + \mathbf{f} \right) \cdot \mathbf{n} \quad (4)$$

In the above,  $\mathbf{n}$  denotes the unit outward normal vector to the domain boundary.

### 3. IMPLEMENTATION OF INCOMPRESSIBLE NAVIER-STOKES EQUATIONS ON NONSTAGGERED GRIDS

While staggered-grid approaches have been used successfully to suppress oscillations arising from even-odd coupling, using them increases the coding complexity and consumes more computational time. This provided motivation for discretizing the partial differential equations over a domain in which both velocities and pressure are stored at the same point. With the nonstaggered mesh, special care must be taken with  $\nabla p$ ; otherwise, spurious oscillations in the pressure field will be inevitable.

The basic idea behind avoiding even-odd decoupling solutions is to employ the nodal value of  $p_j$  when approximating  $\nabla p$  at an interior node  $j$ . Rather than attempting to approximate  $p_x$  at node  $j$  explicitly, the value of  $p_x|_j$  is obtained implicitly along with two adjacent values  $p_x|_{j\pm 1}$ . Define  $F_j$  as

$$F_j = h p_x|_j \quad (5)$$

where  $h$  denotes the uniform mesh size. The method adopted in the present study for solving the above defined nodal value of  $F$  is the following implicit equation:

$$\begin{aligned} \alpha F_{j+1} + \beta F_j + \gamma F_{j-1} = & a(p_{j+2} - p_{j+1}) + b(p_{j+1} - p_j) \\ & + c(p_j - p_{j-1}) + d(p_{j-1} - p_{j-2}) \end{aligned} \quad (6)$$

To determine the seven undetermined coefficients, we start by expanding  $F_{j\pm 1}$  in Taylor series with respect to  $F_j$ , and  $p_{j\pm 1}$  and  $p_{j\pm 2}$  with respect to  $p_j$ . Substituting these expansions into Eq. (6), and using Eq. (5), a simultaneous set of algebraic equations can be obtained for uniquely determining  $\alpha$ ,  $\beta$ ,  $\gamma$ ,  $a$ ,  $b$ ,  $c$ , and  $d$ . On physical grounds, it is legitimate to set  $\alpha = \gamma$ , since  $p$  is elliptic in nature, as revealed by the Poisson equation given in (3). Having set  $\alpha = \gamma$ , other coefficients can be determined as  $\alpha = \frac{1}{5}$ ,  $\beta = \frac{3}{5}$ ,  $a = \frac{1}{60}$ ,  $b = \frac{29}{60}$ ,  $c = \frac{29}{60}$ , and  $d = \frac{1}{60}$ . As for the derivation of a working equation for  $F$  at a node immediately adjacent to the right boundary point (for example), we employ Eq. (6) at the limiting condition of  $\alpha = a = b = 0$ . With the expression for boundary  $F$  via Eq. (6), interior values of  $F_j$  ( $2 \leq j \leq j_{\max} - 1$ ) can be obtained with less computational expense from the banded tridiagonal matrix equations.

### 4. NUMERICAL MODEL

The advection-diffusion schemes have been developed to discretize the one-dimensional transport equation containing convective and diffusive terms. However, it is rather difficult, if not impossible, to develop a truly multidimensional convection-diffusion flux discretization scheme which is not susceptible to false diffusion errors. For this reason, we will resort to the idea of operator splitting, so that calculation can be carried out alternately in each spatial direction. Within this analysis framework, many well-established one-dimensional flux discretization schemes can be applied directly. Besides reducing false diffusion errors, another benefit of applying the ADI scheme is a substantial save of CPU time and disk space.

The ADI solution algorithm we exploit is due to the work of Peaceman and Rachford [26]. Take the following scalar transport equation, which involves constant velocity components  $u$ ,  $v$ , the reaction coefficient  $c$ , and constant diffusion coefficient  $k$ , as an illustrative example,

$$\Phi_t + u\Phi_x + v\Phi_y - k(\Phi_{xx} + \Phi_{yy}) + c\Phi = 0 \quad (7)$$

The use of the ADI solution algorithm permits us to calculate  $\Phi$  via the following two steps.

1. *Predictor step:*

$$\Phi^* + \frac{\Delta t}{2}(u\Phi_x^* - k\Phi_{xx}^* + c\Phi^*) = \Phi^n - \frac{\Delta t}{2}(v\Phi_y^n - k\Phi_{yy}^n) \quad (8)$$

2. *Corrector step:*

$$\Phi^{n+1} + \frac{\Delta t}{2}(v\Phi_y^{n+1} - k\Phi_{yy}^{n+1} + c\Phi^{n+1}) = \Phi^* - \frac{\Delta t}{2}(u\Phi_x^* - k\Phi_{xx}^*) \quad (9)$$

Define  $(\bar{u}, \bar{v}) = (u\Delta t/2, v\Delta t/2)$ ,  $\bar{k} = k\Delta t/2$ , and  $\bar{c} = 1 + c\Delta t/2$ ; the above two-step ADI scheme can then be rewritten as

$$\bar{u}\Phi_x^* - \bar{k}\Phi_{xx}^* + \bar{c}\Phi^* = f_1 \quad (10a)$$

$$\bar{v}\Phi_y^{n+1} - \bar{k}\Phi_{yy}^{n+1} + \bar{c}\Phi^{n+1} = f_2 \quad (10b)$$

In the above, the two source terms  $f_1$  and  $f_2$  are as follows:

$$f_1 = \phi^n - \bar{v}\Phi_y^n + \bar{k}\Phi_{yy}^n \quad (11a)$$

$$f_2 = \phi^* - \bar{u}\Phi_x^* + \bar{k}\Phi_{xx}^* \quad (11b)$$

#### 4.1. Flux Discretization Scheme

As Eqs. (10a) and (10b) show, to obtain an accurate solution for the convection-diffusion equation (7), it is necessary to develop an effective discretization scheme for the following model equation:

$$u\Phi_x - k\Phi_{xx} + c\Phi = f \quad (12)$$

With the aim of suppressing convective instability, we employ the general solution for Eq. (12) as

$$\Phi = a_1 e^{\lambda_1 x} + b_1 e^{\lambda_2 x} + \frac{f}{c} \quad (13)$$

where  $a_1$  and  $b_1$  are constants. Substituting Eq. (13) into Eq. (12), we can derive two equations for  $\lambda_1$  and  $\lambda_2$ . Their expressions are then obtained as follows:

$$\lambda_1 = \frac{u + \sqrt{u^2 + 4ck}}{2k} \quad (14a)$$

$$\lambda_2 = \frac{u - \sqrt{u^2 + 4ck}}{2k} \quad (14b)$$

Derivation of the discrete equation at an interior node  $i$  is followed by use of the following center-like expression:

$$\frac{u}{2h}(\Phi_{i+1} - \Phi_{i-1}) - \frac{m}{h^2}(\Phi_{i+1} - 2\Phi_i + \Phi_{i-1}) + \frac{c}{6}(\Phi_{i-1} + 4\Phi_i + \Phi_{i+1}) = f \quad (15a)$$

or

$$\left(-\frac{u}{2h} - \frac{m}{h^2} + \frac{c}{6}\right)\Phi_{i-1} + 2\left(\frac{m}{h^2} + \frac{c}{3}\right)\Phi_i + \left(\frac{u}{2h} - \frac{m}{h^2} + \frac{c}{6}\right)\Phi_{i+1} = f \quad (15b)$$

Then the exact solutions  $\Phi_i = a_1 e^{\lambda_1 x_i} + b_1 e^{\lambda_2 x_i} + f/c$ ,  $\Phi_{i+1} = a_1 e^{\lambda_1 h} e^{\lambda_1 x_i} + b_1 e^{\lambda_2 h} e^{\lambda_2 x_i} + f/c$ , and  $\Phi_{i-1} = a_1 e^{-\lambda_1 h} e^{\lambda_1 x_i} + b_1 e^{-\lambda_2 h} e^{\lambda_2 x_i} + f/c$  are substituted into Eq. (15b) to derive  $m$  as follows [27]:

$$m = h^2 \left[ \frac{(c/3) + (c/6) \cosh(\bar{\lambda}_1) \cosh(\bar{\lambda}_2) + (u/2h) \sinh(\bar{\lambda}_1) \cosh(\bar{\lambda}_2)}{\cosh(\bar{\lambda}_1) \cosh(\bar{\lambda}_2) - 1} \right] \quad (16)$$

where

$$\bar{\lambda}_1 = \frac{uh}{2k} \quad (17a)$$

$$\bar{\lambda}_2 = \left[ \left(\frac{uh}{2k}\right)^2 + \frac{ch^2}{k} \right]^{1/2} \quad (17b)$$

To shed additional light on the dispersive nature of the above scheme, we consider the model equation in the subsequent dispersion analysis:

$$\Phi_t + u \Phi_x - k \Phi_{xx} = 0 \quad (18)$$

Given the initial condition of  $\Phi(x, t = 0) = \exp(ik_m x)$ , Eq. (18) can be easily shown to have the exact solution given by

$$\Phi(x, t) = \exp(-k k_m^2 t) \exp[ik_m(x - ut)] \quad (19)$$

where  $k_m$  denotes the wave number. With  $h$  ( $\equiv \Delta x$ ) as the mesh size and  $\Delta t$  as the time increment, the discrete equation for (18) is as follows:

$$A\Phi_{i-1}^{n+1} + B\Phi_i^{n+1} + C\Phi_{i+1}^{n+1} = \Phi_i^n \quad (20)$$

In the above,  $A$ ,  $B$ ,  $C$  are expressed as

$$A = -\frac{\bar{m}}{h^2} - \frac{v}{2} + \frac{1}{6} \quad (21)$$

$$B = 2 \left( \frac{\bar{m}}{h^2} + \frac{1}{3} \right) \tag{22}$$

$$C = -\frac{\bar{m}}{h^2} + \frac{v}{2} + \frac{1}{6} \tag{23}$$

where  $v = u \Delta t / h$ . Defining  $Pe = uh/k$ , then  $\bar{m}$  shown in Eqs. (21)–(23) can be expressed as

$$\bar{m} = h^2 \left\{ \frac{(1/3) + (1/6) \cosh(\bar{a}) \cosh(\bar{b}) + (v/2) \sinh(\bar{a}) \cosh(\bar{b})}{\cosh(\bar{a}) \cosh(\bar{b}) - 1} \right\} \tag{24}$$

where

$$\bar{a} = \frac{Pe}{2} \tag{25}$$

$$\bar{b} = \left[ \left( \frac{Pe}{2} \right)^2 + \frac{Pe}{v} \right]^{1/2} \tag{26}$$

Owing to the possible amplitude and phase errors, the exact solution to the finite-difference equation (20) is assumed to take the following form:

$$\Phi(x, t) = \exp \left( -k k_m^2 \frac{k_1}{\alpha^2} t \right) \exp \left[ i k_m \left( x - u \frac{k_2}{\alpha} t \right) \right] \tag{27}$$

where the modified wave number  $\alpha$  is expressed as

$$\alpha = k_m h \tag{28}$$

Dispersion analysis is conducted by substituting  $\Phi_j$  and  $\Phi_{j\pm 1}$ , which are obtained from Eq. (27), into Eq. (20). After some algebra,  $k_1$  and  $k_2$ , which stem from amplitude and phase errors, are derived as

$$k_1 = -\frac{Pe}{v} p \tag{29}$$

$$k_2 = -\frac{q}{v} \tag{30}$$

where  $Pe = uh/k$ ,  $v = u \Delta t / h$ , and

$$q = \tan^{-1} \left[ \frac{(A - C) \sin(\alpha)}{(A + C) \cos(\alpha) + B} \right] \tag{31}$$

$$p = \ln \left\{ \frac{1}{\cos(q)[(A + C) \cos(\alpha) + B] + \sin(q)[(A - C) \sin(\alpha)]} \right\} \tag{32}$$

Upon examination of Figures 1 and 2, which plot  $k_1$  and  $k_2$  against  $Pe$  and  $v$ , we are led to know that  $k_2$  agrees perfectly with  $\alpha$  in the range of low modified wave number. The higher the modified wave number, the less satisfactory is the

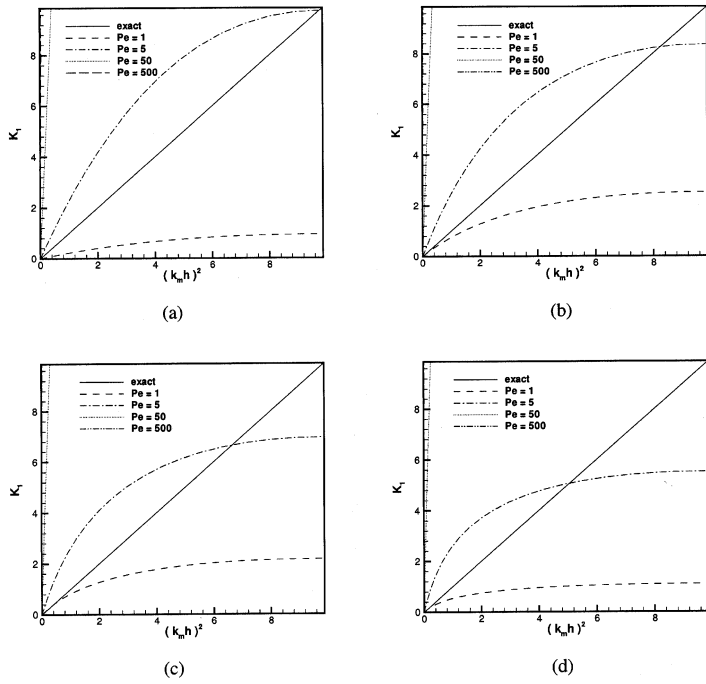


Figure 1. Plots of  $k_1$  against  $Pe$  and  $v$ : (a)  $v = 0.01$ ; (b)  $v = 0.2$ ; (c)  $v = 0.5$ ; (d)  $v = 1.0$ .

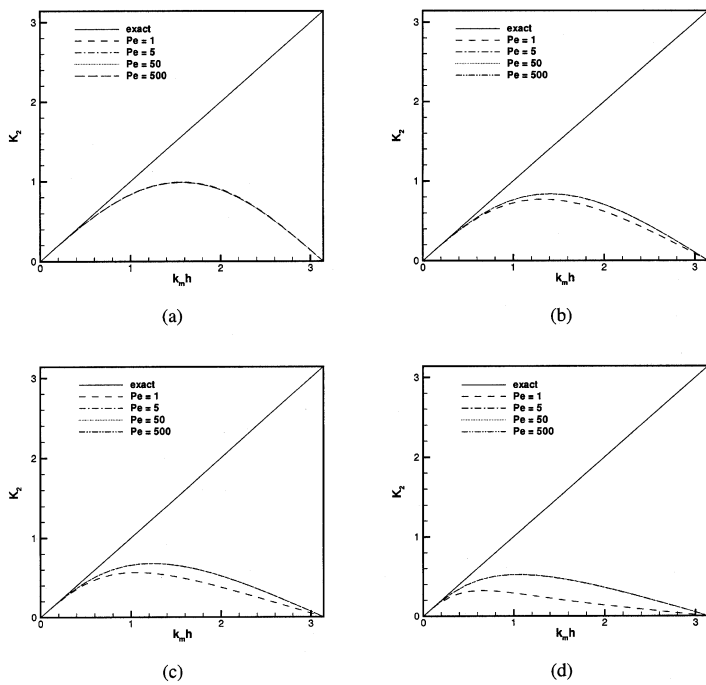


Figure 2. Plots of  $k_2$  against  $Pe$  and  $v$ : (a)  $v = 0.01$ ; (b)  $v = 0.2$ ; (c)  $v = 0.5$ ; (d)  $v = 1.0$ .

performance of the scheme with regard to numerical phase. In contrast to  $k_2$ , amplitude error cannot be well resolved even in the low-wave-number range.

### 4.2. Multidimensional Solution Algorithm

Having developed the discretization scheme for the model Eq. (12), the calculation of  $\Phi^{n+1}$  from Eq. (7) proceeds as follows. Initially, the source term  $f_1$  is calculated using the previous solutions computed at  $t = n \Delta t$ . This is followed by calculating  $\Phi^*$  using the nodally exact one-dimensional CDR scheme. After obtaining the value of  $\Phi^*$ , we can calculate  $f_2$  and then  $\Phi^{n+1}$  using the same CDR scheme employed in the predictor step.

For the sake of accuracy, all the source terms involved in the ADI scheme should be calculated accurately. As an illustrative example, we consider  $\bar{a} > 0$  in the approximation of  $\bar{a} u_x$ . The calculation of  $u_x$  at  $j$  from Eq. (6) proceeds at  $a = 0$ , since the downwind value of  $u$  plays a less important role. Following the same methodology as detailed in Section 3, we can theoretically determine the rest of introduced coefficients and then the value of  $\bar{a} u_x|_j$ .

Throughout this article, the second-derivative terms for the pressure and velocities are approximated in a similar manner. Take  $\Phi_{xx}$  at node  $j$  as an example; the calculation of  $\Phi_{xx}|_j$  starts by assuming  $\Phi_{xx}|_j = S_j/h^2$ . The value of  $S_j$  is then calculated implicitly from

$$h^2 (\bar{\alpha} S_{j+1} + \bar{\beta} S_j + \bar{\gamma} S_{j-1}) = \bar{a}^* \Phi_{j+2} + \bar{b}^* \Phi_{j+1} + \bar{c}^* \Phi_j + \bar{d}^* \Phi_{j-1} + \bar{e}^* \Phi_{j-2} \tag{33}$$

Expanding  $S_{j\pm 1}$  with respect to  $S_j$  and  $\Phi_{j\pm 1}, \Phi_{j\pm 2}$  with respect to  $\Phi_j$  in Taylor series, followed by substituting them into the expression for  $S_j$ , we can obtain eight algebraic equations for  $\bar{\alpha}, \bar{\beta}, \bar{\gamma}, \bar{a}^*, \bar{b}^*, \bar{c}^*, \bar{d}^*$ , and  $\bar{e}^*$ , from which we can get  $(\bar{\alpha}, \bar{\beta}, \bar{\gamma}, \bar{a}^*, \bar{b}^*, \bar{c}^*, \bar{d}^*, \bar{e}^*) = (1, \frac{11}{2}, 1, \frac{3}{8}, 6, -\frac{51}{4}, 6, \frac{3}{8})$ .

Since the CDR scheme developed here is not applicable to the limiting case of  $\mathbf{u} = 0$  and  $c = 0$ , discretization of Eq. (3) should be treated differently. One way to approximate  $p_{xx}$  and  $p_{yy}$  accurately is to adopt Eq. (33), where  $\bar{\alpha}$  and  $\bar{\gamma}$  are assigned to be zero a priori. Other free parameters can be similarly determined using the same method described earlier. The resulting discrete equation for  $\nabla^2 p$  at an interior point  $(i, j)$  reads

$$\nabla^2 p|_{i,j} = p_{i+1,j+1} + p_{i-1,j+1} + p_{i+1,j-1} + p_{i-1,j-1} - 20 p_{i,j} + 4(p_{i+1,j} + p_{i-1,j} + p_{i,j+1} + p_{i,j-1}) \tag{34}$$

The prediction quality for the PPE solution depends highly on the convective term shown on the right-hand side of (4). Depending on the sign of  $u$ , the value of  $u u_x$  at the left boundary is obtained by assuming  $\bar{\alpha} = \bar{\gamma} = 0$  in Eq. (33). The other coefficients are determined as  $\bar{\beta} = 1, \bar{a}^* = -\frac{1}{12}, \bar{b}^* = \frac{4}{3}, \bar{c}^* = -\frac{5}{2}, \bar{d}^* = \frac{4}{3}$  and  $\bar{e}^* = -\frac{1}{12}$ .

### 5. NUMERICAL RESULTS

As is normally the case when a new scheme is presented for solving a differential equation, we will validate the scheme by considering the model equation  $u_t + u_x = \mathbf{D}u_{xx}$ . Subject to the initial condition

$$u(x, t = 0) = \begin{cases} 1; & 0.2 \leq x \leq 0.7 \\ 0; & \text{otherwise} \end{cases} \tag{35}$$

the analytical solution can be derived as

$$u(x, t) = \frac{1}{2} \left[ \operatorname{erf} \left( \frac{x - t - 0.2}{\sqrt{4\mathbf{D}t}} \right) - \operatorname{erf} \left( \frac{x - t - 0.7}{\sqrt{4\mathbf{D}t}} \right) \right] \tag{36}$$

In the above, the error function  $\operatorname{erf}(m)$  is defined as

$$\operatorname{erf}(m) = \frac{2}{\sqrt{\pi}} \int_0^m \exp(-s^2) ds \tag{37}$$

Calculations are carried out at  $\mathbf{D} = 10^{-4}$  and  $\Delta x = \frac{1}{10}, \frac{1}{20}, \frac{1}{40}, \frac{1}{80}$ , and  $\frac{1}{160}$ . For each case, the computed error, cast in its  $L_2$ -error norm form, is plotted by way of  $\log(\text{err}_1/\text{err}_2)$  against  $\log(h_1/h_2)$ , where the errors  $\text{err}_1$  and  $\text{err}_2$  are obtained at  $\Delta x = h_1$  and  $h_2$ . The computed rate of convergence shown in Figure 3a shows good

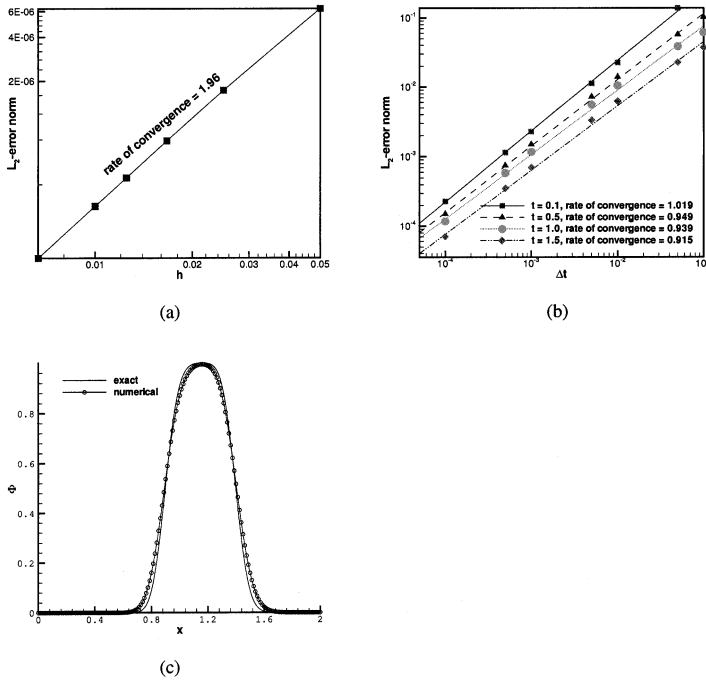


**Figure 3.** Computed results for the inhomogeneous time-dependent convection-diffusion equation considered in Section 5: (a) spatial rate of convergence plot; (b) temporal rates of convergence at different times; (c) solution computed at  $\Delta x = \frac{1}{160}$ .

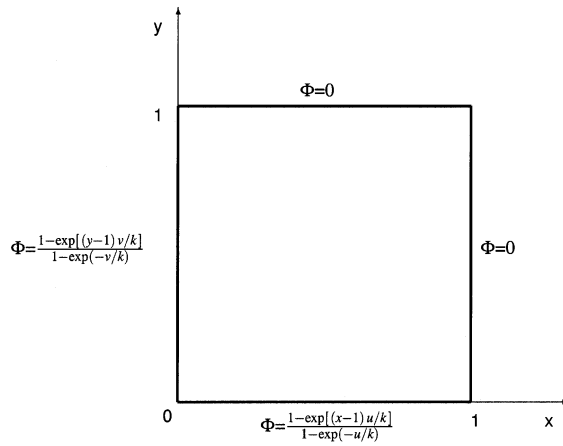


Figure 4. Boundary conditions for the two-dimensional validation test problem.

agreement with its theoretical value shown in Figure 3b and fast convergence to the analytical solution.

After verifying the proposed one-dimensional CDR scheme, we demonstrate proper use of the ADI operator splitting technique by solving the following two-dimensional steady convection-diffusion equation in  $1 \leq x, y \leq 1$ :

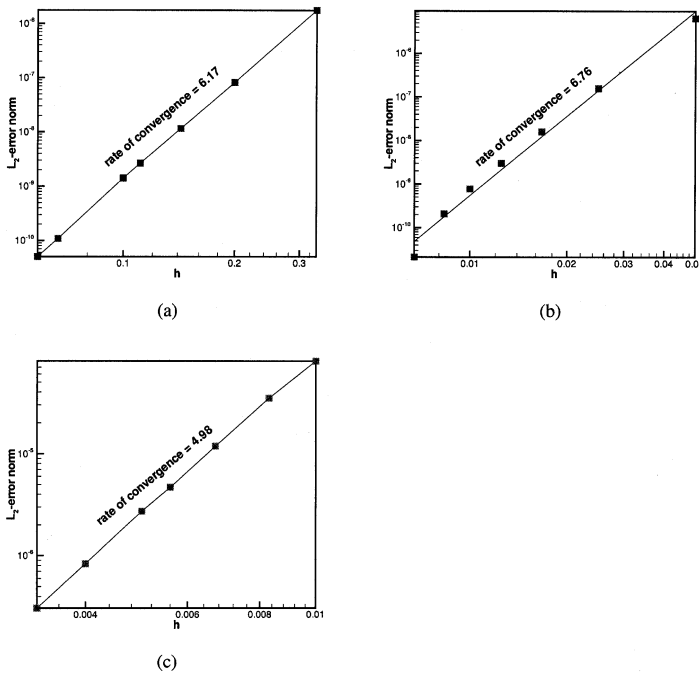


Figure 5. Rate of convergence plots for the two-dimensional scalar transport equation: (a)  $u = v = 1$ ; (b)  $u = v = 10$ ; (c)  $u = v = 100$ .

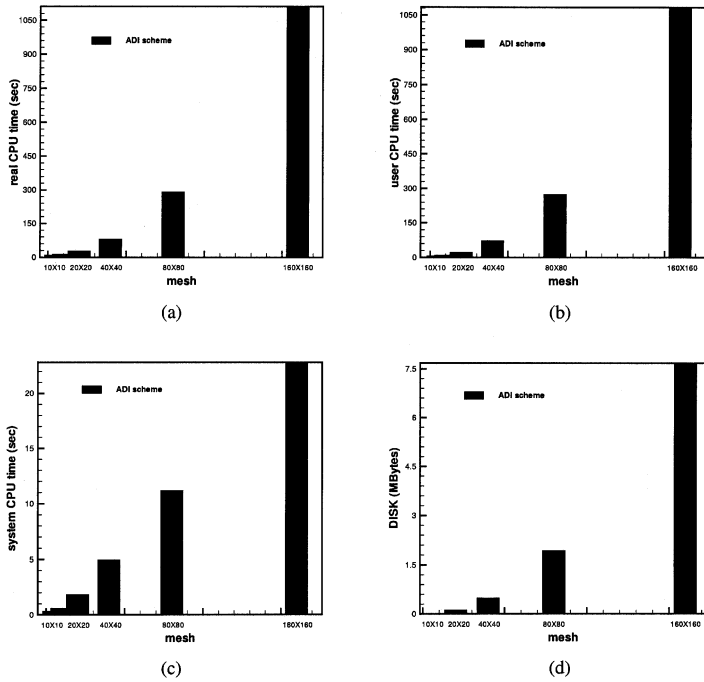


Figure 6. Comparison of disk space and CPU time for the proposed nodally exact finite-difference scheme: (a) real CPU times; (b) user CPU times; (c) system CPU times; (d) disk space.

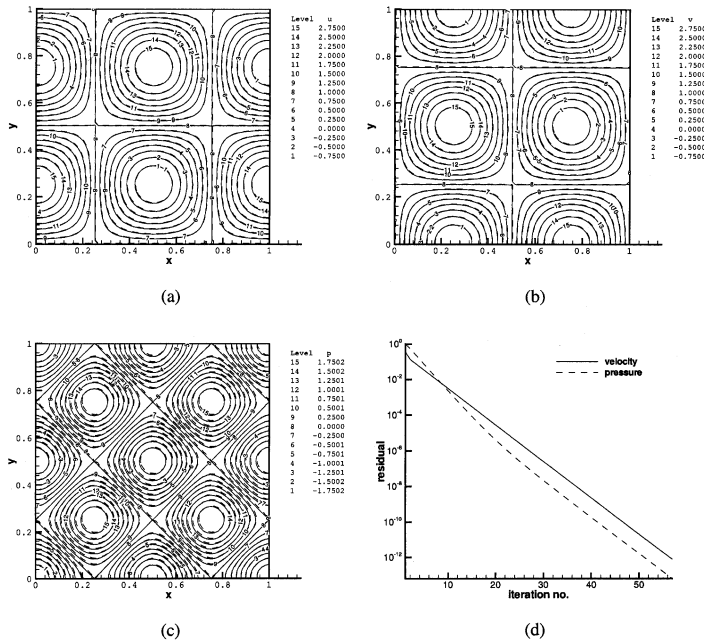


Figure 7. Simulated solutions at  $v = 10^{-2}$  and  $t = 1.0$  (— present solution; - - - exact solution) given in Eq. (40): (a) velocity  $u$ ; (b) velocity  $v$ ; (c) pressure contours; (d) convergence history for the case with  $64 \times 64$  mesh points.

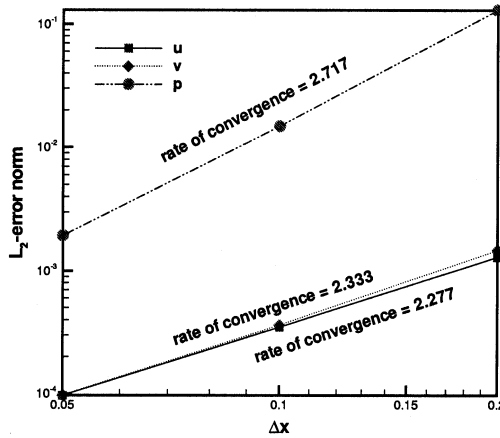


Figure 8. Rates of convergence for the two-dimensional Navier-Stokes problem with solutions given in Eq. (40).

$$u\Phi_x + v\Phi_y = k(\Phi_{xx} + \Phi_{yy}) \tag{38}$$

In the above,  $u$  and  $v$  are constant along the  $x$  and  $y$  directions, respectively. Given the Dirichlet-type boundary conditions shown schematically in Figure 4, the exact solution to the above linearized Burgers equation is given by [28]

$$\Phi(x,y) = \left\{ \frac{1 - \exp[(x - 1)u/k]}{1 - \exp(-u/k)} \right\} \left\{ \frac{1 - \exp[(y - 1)v/k]}{1 - \exp(-v/k)} \right\} \tag{39}$$

Based on the simulated errors obtained at  $\Delta x = \Delta y = \frac{1}{10}, \frac{1}{20}, \frac{1}{40}, \frac{1}{80},$  and  $\frac{1}{160}$ , the rate of convergence is obtained as shown in Figure 5. Good agreement with the theoretical results and fast convergence to the analytical solution are demonstrated.

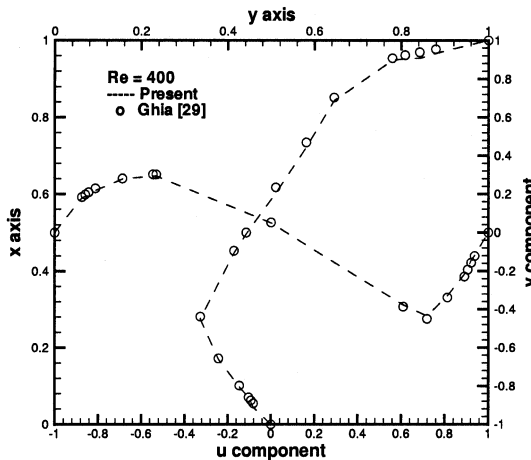


Figure 9. Computed velocity profiles for  $u(x, 0.5)$  and  $v(0.5, y)$  at  $Re = 400$ .

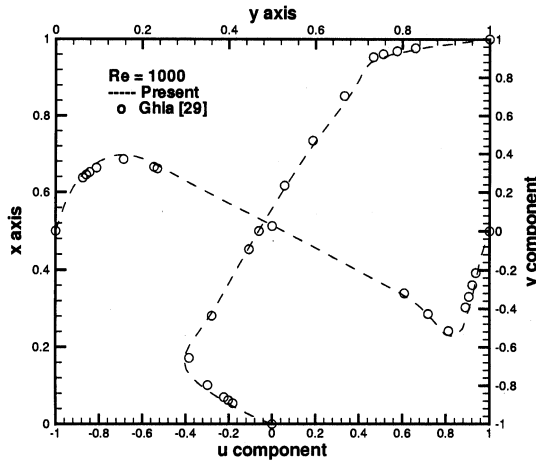


Figure 10. Computed velocity profiles for  $u(x, 0.5)$  and  $v(0.5, y)$  at  $Re = 1,000$ .

For the sake of completeness, both CPU time and disk space used are plotted in Figure 6.

Encouraged by the above success in validating the proposed transport scheme, the Navier–Stokes equations are solved in a unit square. The numerical method is validated using the problem which has the following exact solutions:

$$u = 1 + 2 \cos[2\pi(x - t)] \sin[2\pi(y - t)]e^{-8\pi^2vt} \tag{40a}$$

$$v = 1 - 2 \sin[2\pi(x - t)] \cos[2\pi(y - t)]e^{-8\pi^2vt} \tag{40b}$$

$$p = -\{\cos[4\pi(x - t)] + \cos[4\pi(y - t)]\}e^{-16\pi^2vt} \tag{40c}$$

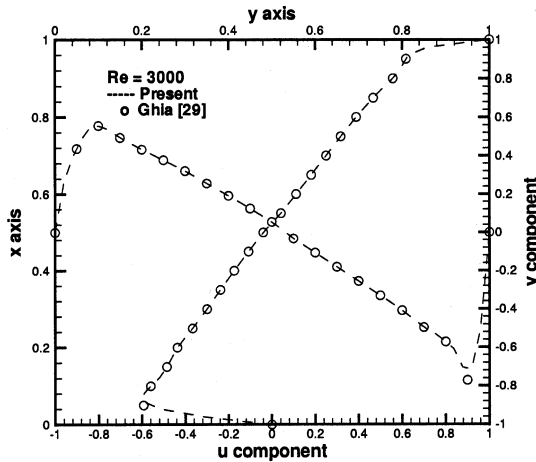


Figure 11. Computed velocity profiles for  $u(x, 0.5)$  and  $v(0.5, y)$  at  $Re = 3,000$ .

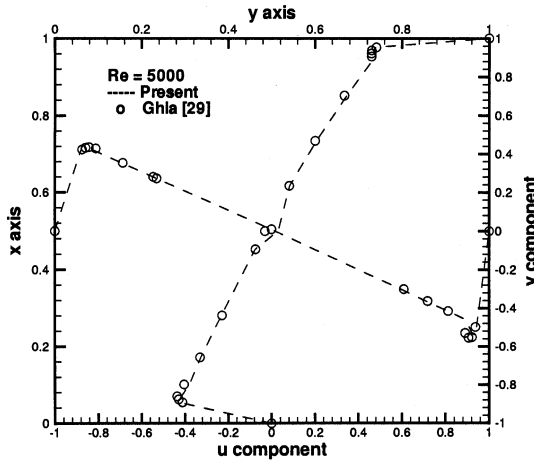


Figure 12. Computed velocity profiles for  $u(x, 0.5)$  and  $v(0.5, y)$  at  $Re = 5,000$ .

All the solutions are obtained in  $0 \leq x, y \leq 1$ . In Figure 7, we plot the simulated contours for  $u$ ,  $v$ , and  $p$  at  $t = 1$ ,  $\nu = 10^{-2}$ ,  $\Delta x = \Delta y = \frac{1}{20}$ , and  $\Delta t = 10^{-2}$ . Computations are also performed on a range of mesh sizes  $h = 1/2^n$ , where  $n = 4, 5, 6, 7$ , at  $\nu = 10^{-2}$ , and  $\Delta t = 1/100$  for the sake of completeness. In view of the  $L_2$ -norm errors plotted in Figure 8, the proposed method is validated.

The flow, which is driven by a constant upper lid velocity  $u_\infty$ , in a square cavity, is then investigated owing to its geometric simplicity but physical complexity. Computations are performed under a range of Reynolds numbers so that we could compare the simulated results with those obtained in the previous computations. With  $L$  as the characteristic length,  $u_{lid}$  as the characteristic velocity, and  $\rho$  as the

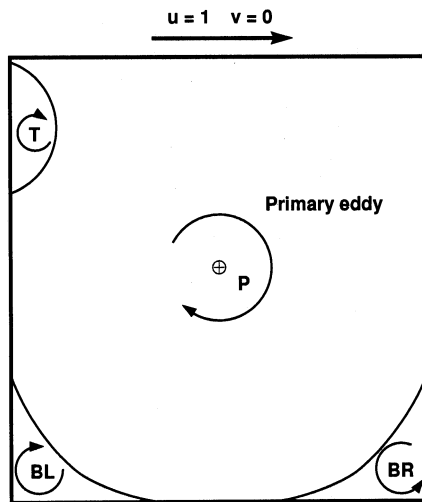


Figure 13. Schematic of the eddy centers.

**Table 1.** Mesh points used and coordinates of the eddy centers (primary eddy P, corner eddies BL and BR, and eddy T near the cavity roof) in the cavity

Symbol	Authors	Re			
		400	1,000	3,000	5,000
Primary	Present	0.5579, 0.6112	0.5331, 0.5745	0.5235, 0.5357	0.5207, 0.5305
	Ghia [29]	0.5547, 0.6055	0.5313, 0.5625	0.5165, 0.5469	0.5117, 0.5352
T	Present	—	—	0.0561, 0.8951	0.0622, 0.8986
	Ghia [29]	—	—	0.0547, 0.8984	0.0625, 0.9141
BL	Present	0.0548, 0.0438	0.0821, 0.0754	0.0835, 0.1097	0.0747, 0.1272
	Ghia [29]	0.0508, 0.0469	0.0859, 0.0781	0.0859, 0.1094	0.0703, 0.1367
BR	Present	0.8807, 0.1261	0.8542, 0.1187	0.9051, 0.0650	0.8048, 0.0726
	Ghia [29]	0.8906, 0.1250	0.8594, 0.1094	0.8125, 0.0859	0.8086, 0.0742
Mesh points	Present	101	131	131	161
	Ghia [29]	257	129	129	257

fluid viscosity, the driven cavity flow problem is investigated at  $Re = 400, 1,000, 3,000,$  and  $5,000$ . It is essential for the mesh to be continuously refined to obtain a grid-independent solution for each test case. The mid-plane velocity profiles  $u(0.5, y)$  and  $v(x, 0.5)$  are plotted in Figures 9–12, and compared with the steady-state benchmark solutions of Ghia [29]. For the sake of completeness, the centers of three eddies at T, BL, and BR are shown schematically in Figure 13. As Table 1 shows, good agreement with the comparison data [29] confirms the applicability of the proposed scheme.

## 6. CONCLUSIONS

A key feature of the present Navier–Stokes method for incompressible fluid flow is its ability to circumvent any spurious pressure oscillation on a nonstaggered grid. This helps to facilitate coding of the program. Another distinct feature of the proposed method is the transformation of the convection-diffusion differential equation into its convection-diffusion-reaction counterpart. For the sake of computational efficiency, the ADI scheme of Peaceman and Rachford is adopted, and the nodally exact one-dimensional scheme can be easily developed from the convection-diffusion-reaction equation. Solution accuracy and stability can be obtained simultaneously. Good agreement between the simulated and analytical solutions is demonstrated for all the test problems. In addition, the spatial rate of convergence is shown to be very high.

## REFERENCES

1. S. V. Patankar, A Calculation Procedure for Two-Dimensional Elliptic Situations, *Numer. Heat Transfer*, vol. 4, pp. 409–425, 1981.
2. S. V. Patankar, *Numerical Heat Transfer and Fluid Flow*, Hemisphere, New York, 1980.
3. J. Papageorgakopoulos, G. Arampatzis, D. Assimacopoulos, and N. C. Markatos, Enhancement of the Momentum Interpolation Method on Non-staggered Grids, *Int. J. Numer. Meth. Fluids*, vol. 33, pp. 1–12, 2000.

4. F. H. Harlow and J. E. Welch, Numerical Calculation of Time-Dependent Viscous Incompressible Flow of Fluid with Free Surface, *Phys. Fluids*, vol. 8, pp. 2182–2189, 1965.
5. C. M. Rhie and W. L. Chow, Numerical Study of the Turbulent Flow past an Airfoil with Trailing Edge Separation, *AIAA J.*, vol. 21, pp. 1525–1532, 1983.
6. T. Gjesdai and M. E. H. Lossius, A General Algorithm for Compressible and Incompressible Flow, *Int. J. Numer. Meth. Fluids*, vol. 25, pp. 393–405, 1997.
7. S. K. Choi, H. Y. Nam, and M. Cho, Use of the Momentum Interpolation Method for Numerical Solution of Incompressible Flows in Complex Geometries, *Numer. Heat Transfer B*, vol. 23, pp. 21–41, 1993.
8. T. F. Miller and F. W. Schmidt, Use of a Pressure-Weighted Interpolation Method for the Solution of Incompressible Navier–Stokes Equations on a Nonstaggered Grids System, *Numer. Heat Transfer*, vol. 14, pp. 213–233, 1988.
9. M. C. Melaaen, Analysis of Fluid-Flow in Constricted Tubes and Ducts Using Body-Fitted Non-staggered Grids, *Int. J. Numer. Meth. Fluids*, vol. 15, pp. 895–923, 1992.
10. R. W. Yeo, P. E. Wood, and A. N. Hrymak, A Numerical Study of Laminar 90-Degree Bend Duct Flow with Different Discretization Schemes, *Trans. ASME, J. Fluids Eng.*, vol. 113, pp. 563–568, 1991.
11. S. W. Armfield, Finite Difference Solutions of the Navier–Stokes Equations on Staggered and Non-staggered Grids, *Comput. Fluids*, vol. 20, pp. 1–17, 1991.
12. T. Han, Computational Analysis of Three-Dimensional Turbulent Flow around a Bluff Body in Ground Proximity, *AIAA J.*, vol. 27, pp. 1213–1219, 1989.
13. P. J. Coelho and J. C. F. Pereira, Finite Volume Computation of the Turbulent-Flow over a Hill Employing 2D or 3D Non-orthogonal Collocated Grid Systems, *Int. J. Numer. Meth. Fluids*, vol. 14, pp. 423–441, 1992.
14. I. E. Barton and R. Kirby, Finite Difference Scheme for the Solution of Fluid Flow Problems on Non-staggered Grids, *Int. J. Numer. Meth. Fluids*, vol. 33, pp. 939–959, 2000.
15. A. W. Date, Solution of Navier–Stokes Equations on Non-staggered Grids, *Int. J. Heat Mass Transfer*, vol. 36, pp. 1913–1922, 1993.
16. G. D. Thiant, Finite Difference Scheme for the Numerical Solution of Fluid Flow and Heat Transfer Problems on Non-staggered Grids, *Numer. Heat Transfer B*, vol. 17, pp. 43–62, 1990.
17. G. E. Schneider and M. J. Raw, Control Volume Finite-Element Method for Heat Transfer and Fluid Flow Using Collocated Variables—1. Computational Procedure, *Numer. Heat Transfer*, vol. 11, pp. 363–390, 1987.
18. G. B. Deng, J. Piquet, P. Queutey, and M. Visonneau, A New Fully Coupled Solution of the Navier–Stokes Equations, *Int. J. Numer. Meth. Fluids*, vol. 19, pp. 605–639, 1994.
19. G. B. Deng, J. Piquet, P. Queutey, and M. Visonneau, Incompressible Flow Calculations with a Consistent Physical Interpolation Finite Volume Approach, *Comput. Fluids*, vol. 23, pp. 1029–1047, 1994.
20. M. Peric, R. Kessler, and G. Scheuerer, Comparison of Finite-Volume Numerical Methods with Staggered and Colocated Grids, *Comput. Fluids*, vol. 16, pp. 389–403, 1988.
21. M. C. Melaaen, Calculation of Fluid Flows with Staggered and Nonstaggered Curvilinear Nonorthogonal Grids—A Comparison, *Numer. Heat Transfer B*, vol. 21, pp. 21–39, 1992.
22. M. M. T. Wang and Tony W. H. Sheu, An Element-by-Element BICGSTAB Iterative Method for Three-Dimensional Steady Navier–Stokes Equations, *J. Comput. Appl. Math.*, vol. 79, pp. 147–165, 1997.
23. P. M. Gresho and R. L. Sani, On Pressure Boundary Conditions for the Incompressible Navier–Stokes Equations, *Int. J. Numer. Meth. Fluids*, vol. 7, pp. 1111–1145, 1987.
24. L. Quartapelle and M. Napolitano, Integral Conditions for the Pressure in the Computation of Incompressible Viscous Flows, *J. Comput. Phys.*, vol. 62, pp. 340–348, 1986.

25. Tony W. H. Sheu, M. M. T. Wang, and S. F. Tsai, Pressure Boundary Conditions for a Segregated Approach to Solving Incompressible Navier–Stokes Equations, *Numer. Heat Transfer B*, vol. 34, pp. 457–467, 1998.
26. D. W. Peaceman and H. H. Rachford, The Numerical Solution of Parabolic and Elliptic Differential Equations, *J. SIAM*, vol. 3, pp. 28–41, 1955.
27. Tony W. H. Sheu, S. K. Wang, and R. K. Lin, An Implicit Scheme for Solving the Convection-Diffusion-Reaction Equation in Two Dimensions, *J. Comput. Phys.*, vol. 164, pp. 123–142, 2000.
28. M. M. Rai and D. A. Anderson, Application of Adaptive Grids to Fluid Flow Problems with Asymptotic Solutions, *AIAA J.*, vol. 20, pp. 496–502, 1982.
29. U. Ghia, K. N. Ghia, and C. T. Shin, High- $Re$  Solutions for Incompressible Flow Using the Navier–Stokes Equations and a Multigrid Method, *J. Comput. Phys.*, vol. 48, pp. 387–411, 1982.